Interference-Free Detection of Genetic Biomarkers Using Synthetic Dipole-Facilitated Nanopore Dielectrophoresis

Kai Tian, Karl Decker, Aleksei Aksimentiev, and Li-Qun Gu

Supplementary Information

Table S1. Amino acid and nucleotide sequences of the nanocarrier and nucleic acid targets

Figure S1-S15

Supplementary Methods 1: Materials, long RNA synthesis and processing, and single channel recording

Supplementary Methods 2: MD protocols

Supplementary Methods 3: Theoretical model of nanopore dielectrophoresis

Table S1. Amino acid and nucleotide sequences of the nanocarriers and nucleic acid targets

Nanocarrier or Target	Sequences
Carrier1	N′-YGRKKRRQRRR-AACCACACAA-C′
D10	$\qquad$ │││││││││ 3′-<u>TTGGTGTGTT</u>-5′
D22	3′-<u>TTGGTGTGTT</u>GGATGATGGAGT-5′
D30	3′-<u>TTGGTGTGTT</u>GGATGATGGAGT(TAC)$_2$TA-5′
D40	3′-<u>TTGGTGTGTT</u>GGATGATGGAGT(TAC)$_6$-5′
D50	3′-<u>TTGGTGTGTT</u>GGATGATGGAGT(TAC)$_9$T-5′
D60	3′-<u>TTGGTGTGTT</u>GGATGATGGAGT(TAC)$_{12}$TA-5′
D70	3′-<u>TTGGTGTGTT</u>GGATGATGGAGT(TAC)$_{16}$-5′
D80	3′-<u>TTGGTGTGTT</u>GGATGATGGAGT(TAC)$_{19}$T-5′
D90	3′-<u>TTGGTGTGTT</u>GGATGATGGAGT(TAC)$_{22}$TA-5′
D90-SNP [a]	3′-<u>TTGGT**A**TGTT</u>GGATGATGGAGT(TAC)$_{22}$TA-5′
dsD80	5′-CCTACTACCTCA(ATG)$_{22}$AT-3′ ││││││││││││││││││││││││ 3′-<u>TTGGTGTGTT</u>GGATGATGGAGT(TAC)$_{22}$TA-5′
DM50	3′-(C)$_{22}$<u>TTGGTGTGTT</u>GGATGATGGAGT(C)$_{10}$-5′
G-Quadruplex [b]	3′-<u>TTGGTGTGTT</u>TACTAC<u><u>GGTTGGTGTGGTTGG</u></u>-5′
Let-7b (miRNA)	3′-<u>uugguguguu</u>ggaugauggagu
Carrier2	N′-YGRKKRRQRRR-CACACTAGGA-C′
APOC1 (mRNA)	$\qquad$ ││││││││││ 3′-<u>gugugauccu</u>uuucacaucguaucacuguaacgauccgacg-5′
Carrier3 [c]	N′-RRRQRRKKR-O-O-CTATCACGATTAGCATTA-C′
miR-155 (miRNA)	$\qquad$ ││││││││││││││││││ 3′-ugggg<u>auagugcuaaucguaauu</u>-5′

[a]: D90-SNP contain a different nucleotide from D90, thus forms a single mismatched base-pair with Carrier1.

[b]: The double underlined sequence forms a G-quadruplex tertiary structure

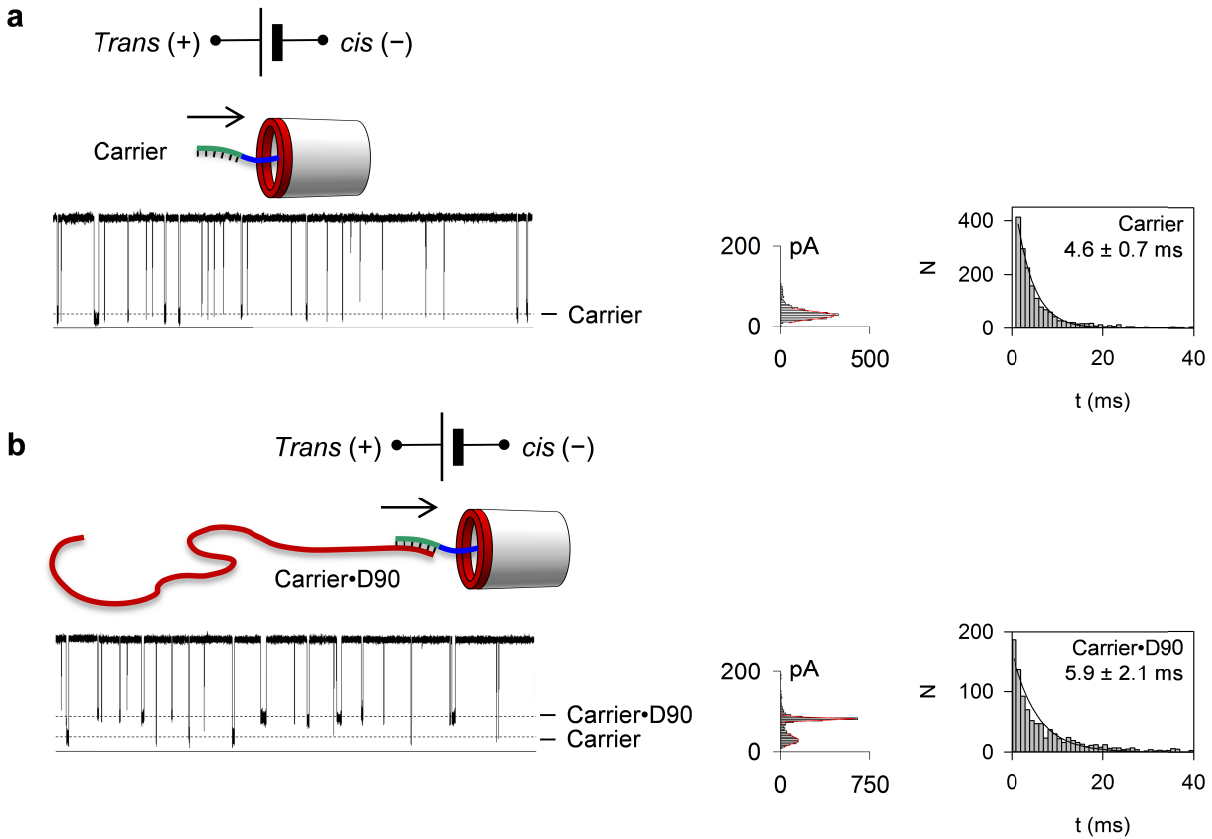[c]: This nanocarrier is a microRNA inhibitor obtained from Panagene Inc.

a

Trans (+) ●—|■|—● cis (−)

Carrier

— Carrier

200 pA

0

0   500

400

N 200

0

Carrier
4.6 ± 0.7 ms

0   20   40

t (ms)

b

Trans (+) ●—|■|—● cis (−)

Carrier•D90

— Carrier•D90
— Carrier

200 pA

0

0   750

200

N 100

0

Carrier•D90
5.9 ± 2.1 ms

0   20   40

t (ms)

Figure S1. a and **b**, Representative ionic current traces (left) and histograms of blockade current amplitudes (center) and blockade durations (right) produced by free Carrier1 (a) and the Carrier1•D90 complex (Table S1 for sequences of Carrier1 and D90). The current through the open K131D$_7$ pore at +180 mV is I_0=292±10 pA. The average current level and duration of Carrier1 signatures (panels a and b) are I=27±1 pA and τ_{off}=4.6±0.7 ms. The current level and duration of Carrier1•D90 signatures (panel b) are I=83±3 pA and τ_{off}=5.9±2.1 ms.
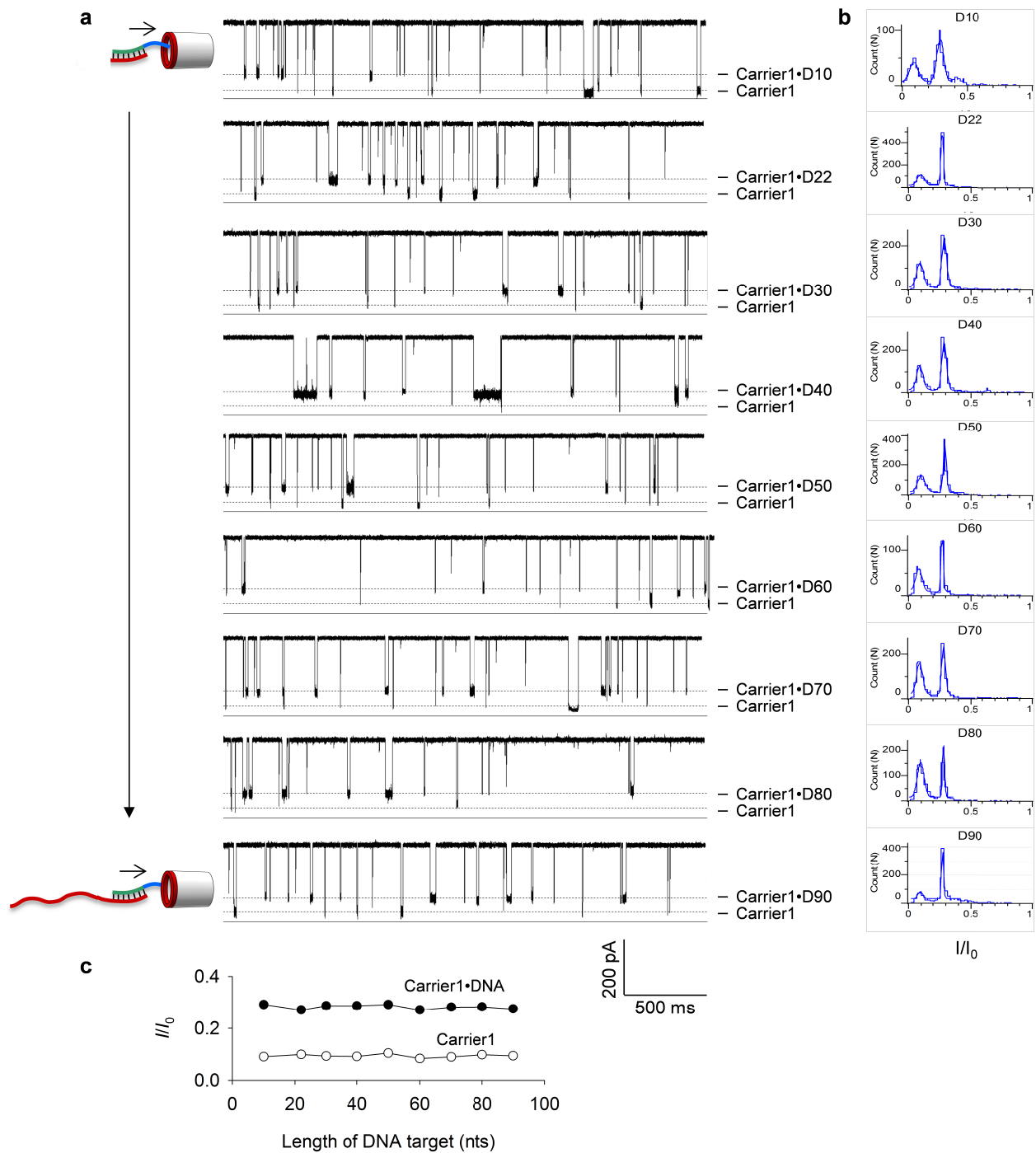
Figure S2. Capture of carrier•DNA complexes by the nanopore for DNA targets of various lengths. **a.** Current traces recorded at +180 mV for a mixture of Carrier1 (100 nM) and various length target DNAs (100 nM), including D10, D22, D30, D40, D50, D60, D70, D80 and D90 (Table S1). The blocking levels for Carrier1 translocating through the pore and Carrier1•DNA

4

complexes captured by are marked. **b.** Histograms of blocking level magnitudes. Blocking level is defined as I/I_0, where I and I_0 are the current amplitudes of the blockade and the open K131D pore, respectively. The component of $I/I_0 \sim 10\%$ was for translocation of free Carrier1, and the $I/I_0 \sim 27\text{-}29\%$ component was generated by the Carrier•DNA complex captured by the pore. **c.** Blocking levels for free Carrier1 and carrier•DNA complexes at various DNA lengths. Each blocking level was obtained by Gaussian fitting of the histograms shown in b. Regardless of the length of the DNA target, the carrier•DNA complexes block the ionic current to a higher level than Carrier1 alone. All carrier•DNA complexes can be captured from the *trans* side with the carrier entering the K131D$_7$ pore from the *trans* entrance.
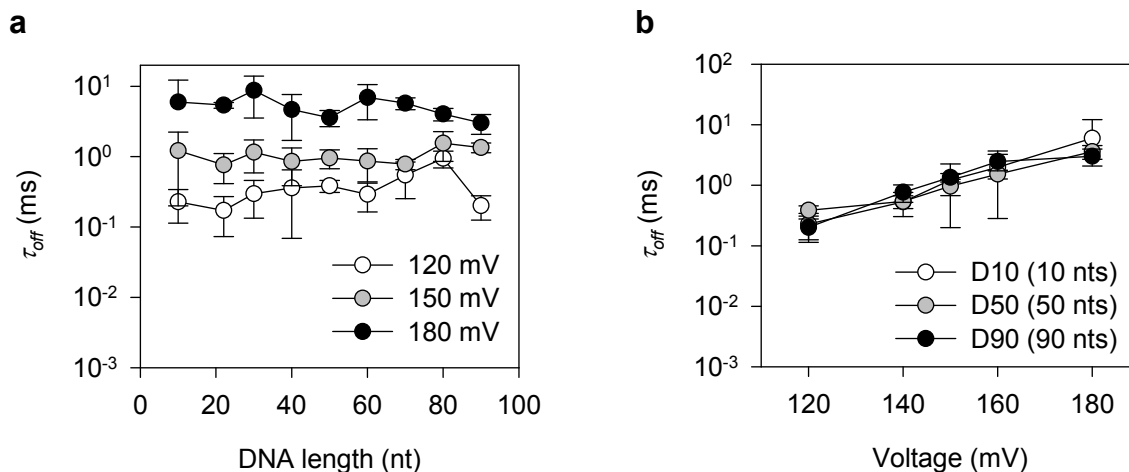
Figure S3. Duration (τ_{off}) of the carrier•DNA blockade signatures as a function of DNA length and voltage. **a,** Variation of τ_{off} with the DNA length at +120 mV, +150 mV and +180 mV. τ_{off} is independent of the DNA length. **b,** Variation of τ_{off} with the voltage for the following DNA constructs: D10 (10 nts), D50 (50 nts) and D90 (90 nts). τ_{off} increases with increasing the voltage, implying that the carrier•DNA complex captured by the nanopore does not translocate through the pore but remains trapped near the pore entrance with its peptide domain inserted into the stem of pore and the PNA:DNA duplex domain remaining outside the pore. The histograms of the blockade durations for each experimental condition are shown in Fig. S4.
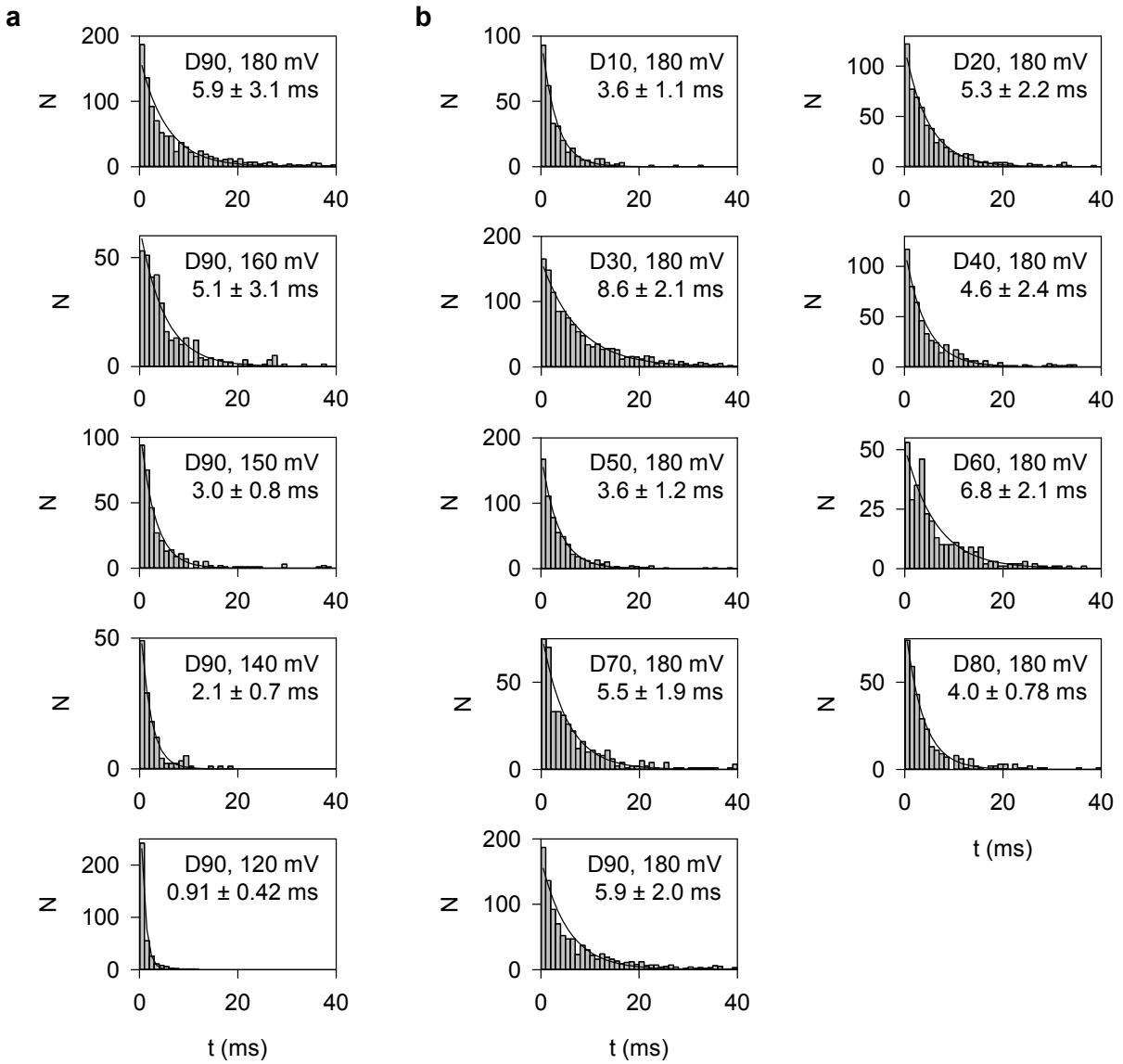
Figure S4. Histograms of blockade duration recorder for various Carrier1•DNA constructs at several values of the transmembrane voltage. **a,** Histograms produced by the Carrier1•D90 complex at several voltages ranging from 120 mV to 180 mV. **b,** Histograms produced by Carrier1 in complex with DNA of several lengths (D10-D90).
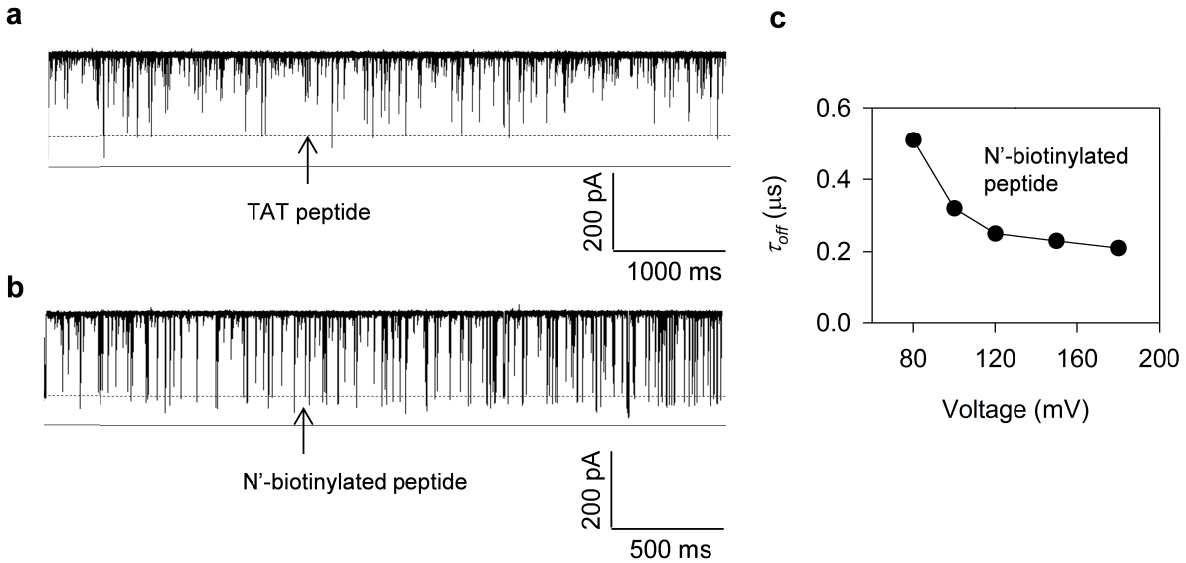
Figure S5. Ionic current traces generated by translocation of the polycationic peptide tag of the nanocarrier through the $K131D_7$ pore from the *trans* entrance. The sequence of the peptide was N'-YGRKKRRQRRRG-C' (Table S1). A 320 nM solution of the peptide was presented to the *trans* chamber; the nanopore current was monitored at +180 mV. **a,** Blockades of ionic current produced by the unmodified peptide. The blockade levels have a broad distribution with the deepest blockade being at I/I_0=27%; **b,** Blockades of ionic current produced by the N'-biotinylated synthetic peptide. Most of the current blocks produced by this terminal-modified peptide are at the I/I_0=21% level; **c,** The duration of the blockades (τ_{off}) shortens as the voltage increases, suggesting that this peptide can translocate through the pore driven by the transmembrane voltage. Importantly, the carrier•DNA complex reduced the nanopore current to the similar current level (Fig. S1), supporting our interpretation of such blockade events as having the carrier•target complex captured by the nanopore, its peptide tag pulled into the pore stem, and the PNA-target duplex left outside the pore entrance.
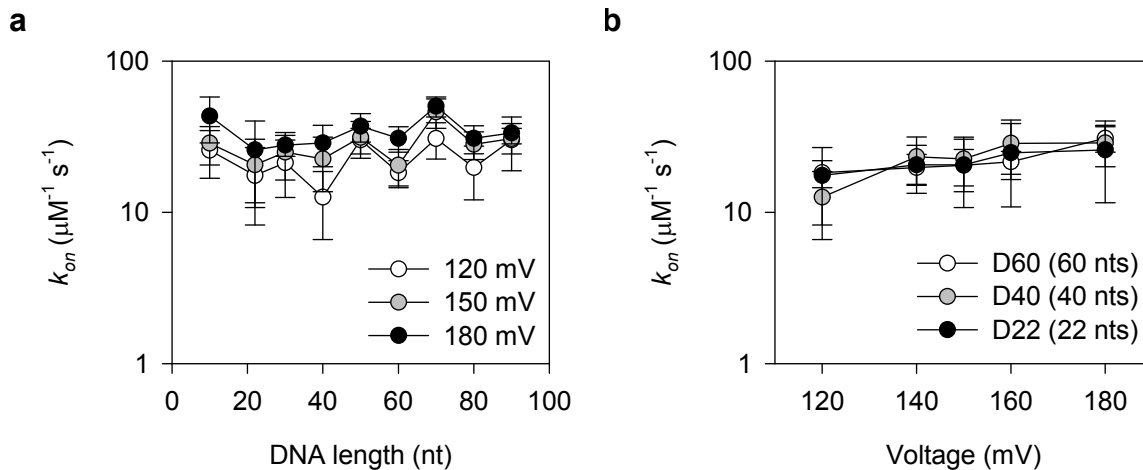
Figure S6. Capture rate (k_{on}) of a carrier•DNA complex as a function of the DNA length and voltage. **a,** Variation of k_{on} with the DNA length at 120 mV, 150 mV and 180 mV. k_{on} is independent of the DNA length. **b,** Variation of k_{on} with the voltage for the following DNA constructs: D10 (10 nts), D50 (50 nts) and D90 (90 nts). k_{on} slightly increases with voltage.
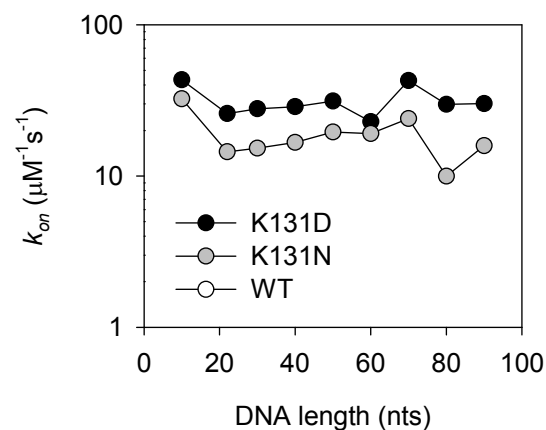
Figure S7. Capture rate (k_{on}) of the carrier•DNA complex for the K131D$_7$, K131N$_7$ and WT pores as a function of the DNA length. k_{on} for the K131D$_7$ pore (charge $-21e$), was higher than that for the less negatively charged K131N pore ($-14e$). k_{on} for the least negatively charged WT pore ($-7e$) was zero (recorded for 5 minutes) for all DNA constructs. Thus, the negative charge at the pore entrance increases the rate of the carrier•DNA complex capture.
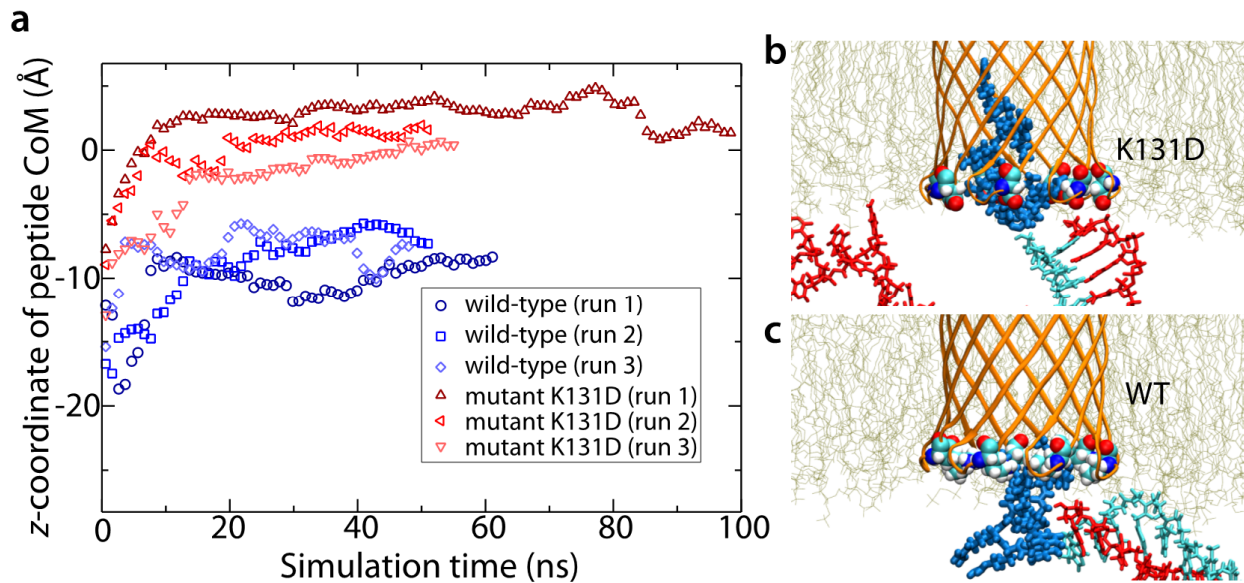
Figure S8. a, MD simulation of the carrier•DNA capture by the WT and K131D$_7$ variants of αHL. The z-coordinate of the peptide tag's center of mass (CoM) is plotted versus simulation time. Three independent simulations were performed for each pore variant. Runs 1 and 2 began from the configuration shown in Fig. 2a at t=0 ns. In run 3, the carrier•DNA complex was initially placed 4 Å further away from the nanopore than in runs 1 and 2. The peptide tag was observed to enter the stem of alpha-hemolysin only for the K131D$_7$ variant of the channel. **b** and **c,** Typical conformations of the peptide tag (blue licorice) at the end of the capture simulations for K131D$_7$ (c) and WT (d) variants of the channel. For clarity, only a part of the simulation system is shown. PNA is rendered in teal licorice, DNA in red licorice, the and αHL in orange cartoon; residues 131 targeted for mutation at the αHL lumen are shown as colored spheres, with oxygen red, carbon cyan, nitrogen blue, and hydrogen white. Lipid bilayer is shown as tan lines.
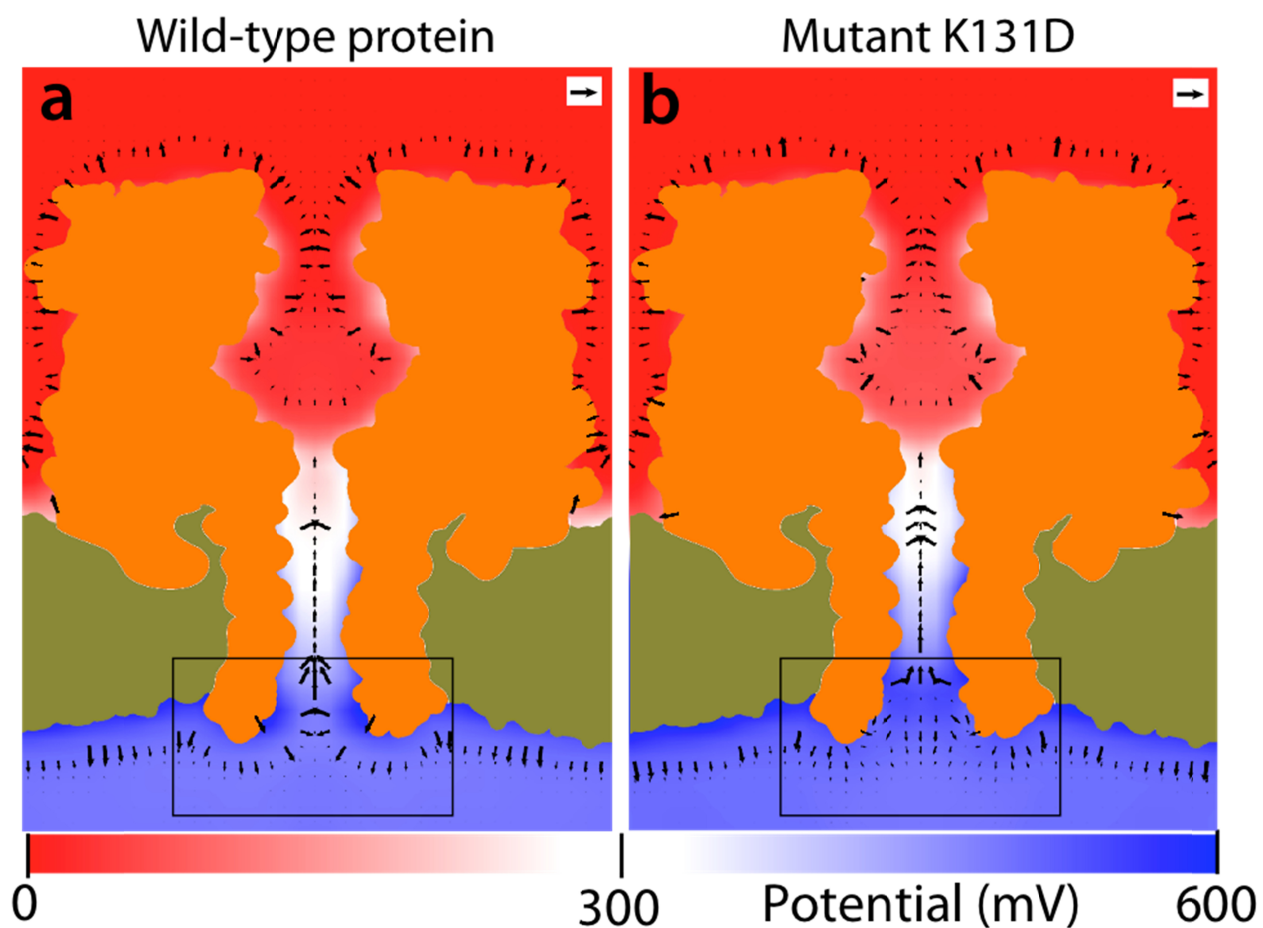
Figure S9. The distribution of the electrostatic potential (color) and the magnitude and direction of the local electrostatic force on one proton charge (arrows) in the open-pore K131D and WT systems at a 600 mV bias. The force scale bar (arrow in the top right corners of the panel) indicates a 3pN force. αHL and lipid bilayer are shown as orange and olive silhouettes respectively. Electric potentials were calculated by analyzing the corresponding MD trajectories using the PMEPOT plugin of VMD; the resulting 3D maps were cylindrically averaged with respect to the pore axis. The local electrostatic forces were calculated as derivatives of the electrostatic potential multiplied by the charge of a proton. The black rectangle indicates the region used for the calculation of the force difference map produced by the change of the nanopore charge (Fig. 2d).
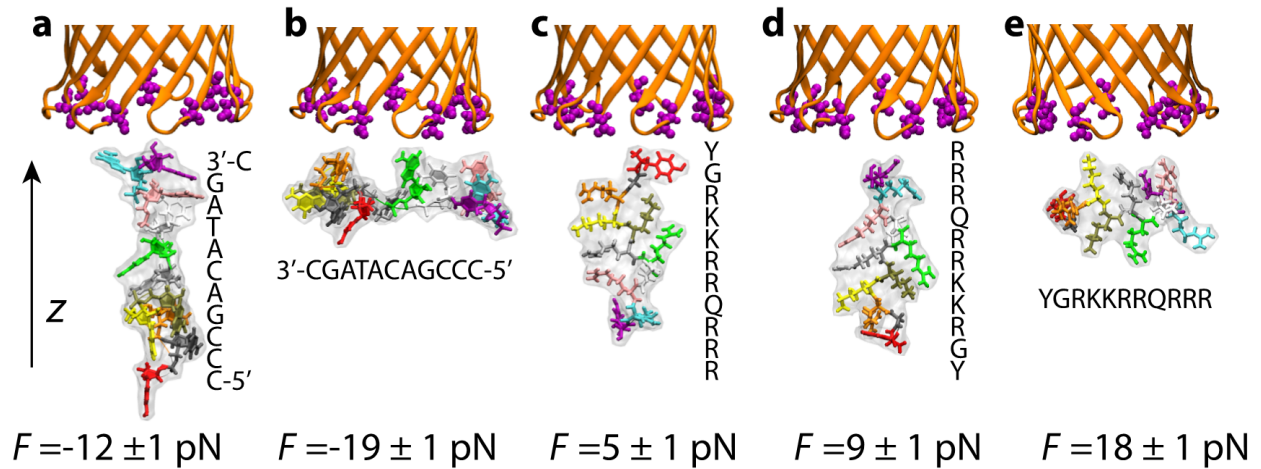
Figure S10. SMD simulations of the effective force on the components of the carrier•DNA complex: 11-nucleotide ssDNA of total charge $-11e$ (a, b) and 11-amino acid peptide tag of total charge $+8e$ (c-e). The *trans* side of the stem of αHL is shown as ribbons, the 131 residues as purple spheres, and the probes as molecular bonds with each residue shown in unique color. A semi-transparent molecular surface indicates the approximate physical volume occupied by the probe. Each system containing a probe and the K131D$_7$ variant of the channel was simulated for 25 ns under a 1.2 V transmembrane bias. The resulting average forces were -12 ± 1 pN (a), -19 ± 1 pN (b), $+5\pm1$ pN (c), $+9\pm1$ pN (d) and $+18 \pm 1$ pN (e). For clarity, only select parts of the system are shown.
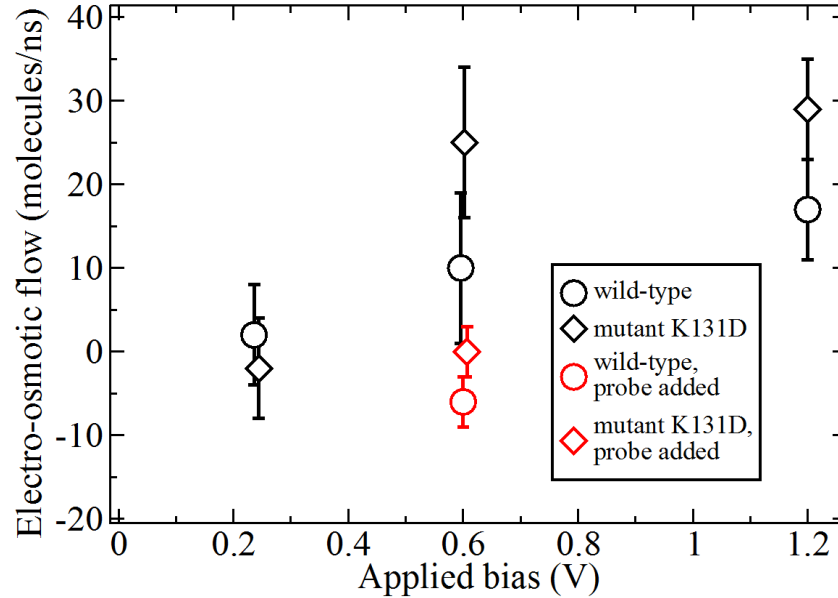
Figure S11. Electro-osmotic flow as a function of the applied bias for αHL systems, with and without a peptide tag added. A positive value indicates water movement from the αHL lumen to the cap. For clarity, some symbols have been offset slightly on the horizontal axis to reduce overlap. In both WT and K131D$_7$ systems, the transmembrane voltage induced a water flow through an open pore directed from *trans* to *cis* sides of the membrane. If any, the effect of the viscous drag would be to increase the attractive force on the probe. The presence of the peptide tag modified the flow pattern, abolishing the flow in the case of the K131D$_7$ mutant and reversing the direction of the flow in the case of the WT. To directly characterize the effect of the electroosmotic flow on the effective force, we repeated simulations of the WT/peptide tag system, blocking the flow through the channel by harmonic restraints on water molecules within the stem of the nanopore. If viscous drag contributed meaningfully to the effective force, blocking the flow should have significantly decreased the effective force. The resulting trajectories showed a slight but not significant decrease (Fig. 2e) in the effective force in the WT system, suggesting that electroosmosis does not play a considerable role in the mechanism of the carrier•DNA capture.
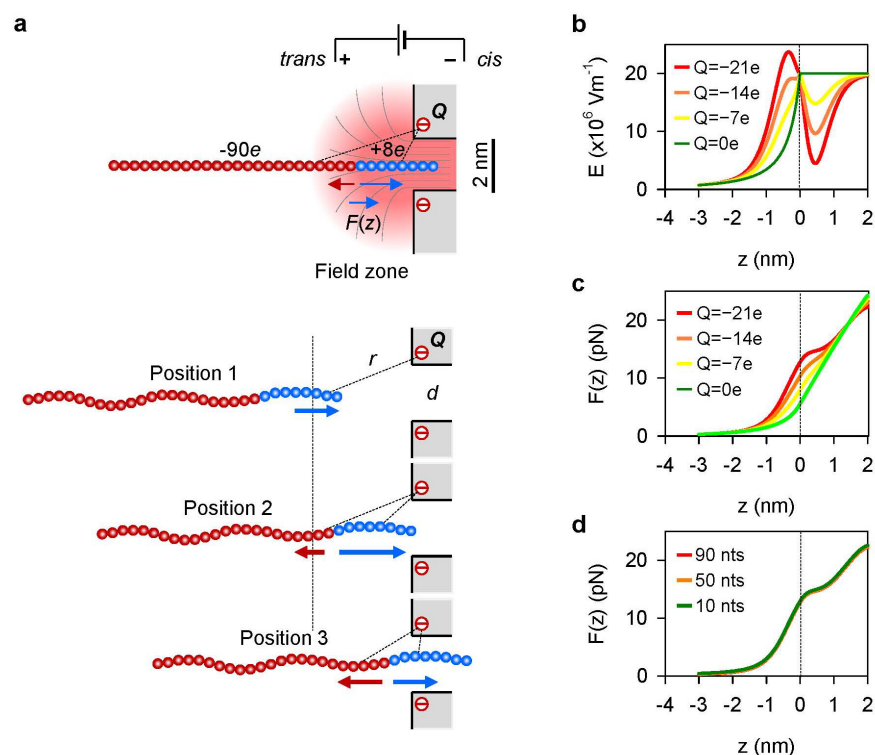
Figure S12. Mechanism of nanopore dielectrophoresis for capturing carrier•DNA complex in a non-uniform electric field. **a,** Schematics of a model for capturing the carrier (blue circles)•DNA (red circles) complex from the bulk solution into the nanopore. The complex position (z-coordinate of 1st positively charged residue of the carrier), and the corresponding field strength (panel b) and the effective force (panel c) are marked. Color arrows indicate the direction and relative amplitude (arrow length) of the forces acting on the cationic peptide (blue arrows) and anionic DNA (red arrows) as the carrier•DNA complex moves toward the pore. **b,** The projection of the electric field onto the z axis along the z axis for several pore models differentiated by the charge at the pore entrance (Q). The $z<0$ and $z>0$ regions are located outside and inside the pore, respectively. $E(z)$ has two components, the field contributed by the pore charge, $E_Q(z)$, and the field contributed by the transmembrane bias, $E_V(z)$ (see Supplementary Methods 3). $Q=-21e$, $-14e$, $-7e$ and $0e$ represent the K131D$_7$, K131N$_7$ and WT variants of the pore and a pore with a

neutral entrance. **c,** Effective force Fz acting on the carrier•D90 complex along the z-axis and its dependence on the pore charge Q. The carrier•D90 complex was modeled as a string of 8 positive charges (for the peptide module) linked to 90 negative charges (for ssDNA). Fz was the sum of the forces acting on each charge in the electric field $E(z)$. The expression for Fz is derived in Supplementary Methods 3. **d,** Effective force Fz acting on the carrier•DNA complex for DNA targets of different length. Because our model does not consider the steric reaction force on the complex from the pore, the force does not drop to zero when the carrier•DNA complex is lodged at the rim of the pore, as seen in our MD simulations (Fig. 2c).
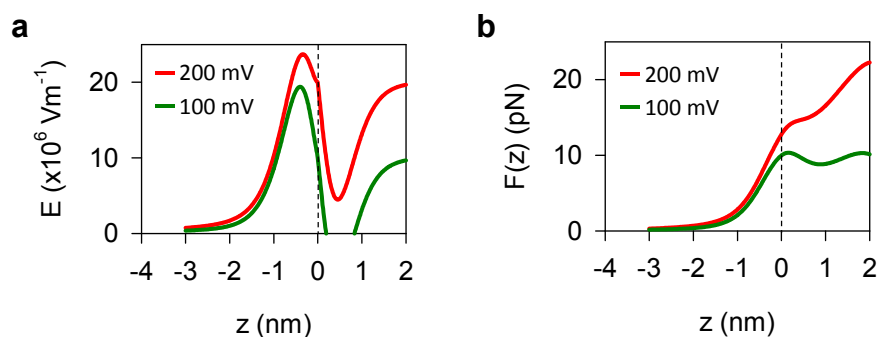
Figure S13. Theoretical model of the electric field intensity and effective force acting on the carrier•DNA complex at +100 mV and +200 mV. **a,** Electric field intensity was calculated using Eqs.S4-S6. **b,** Force acting on the carrier•DNA complex calculated using Eqs. S7-S9. The carrier contains 8 positively charged residues (+8e), and DNA contains 90 nucleotides (−90e). The result shows that $F(z)$ at $z<0$ does not significantly change with voltage, whereas $F(z)$ at $z>0$ does. This finding suggests that the relatively low voltage (<200 mV) plays a minor role in attracting the carrier•DNA complex from bulk solution to the pore ($z<0$), but once captured in the pore ($z>0$), the force to hold the carrier•DNA complex increases with the voltage. This property explained why the carrier•DNA capture rate (k_{on}) was not significantly affected by voltage (Fig. S6b), whereas the duration of the carrier•DNA signature blockade (the capture time, τ_{off}) increased with voltage applied (Fig. S3b).
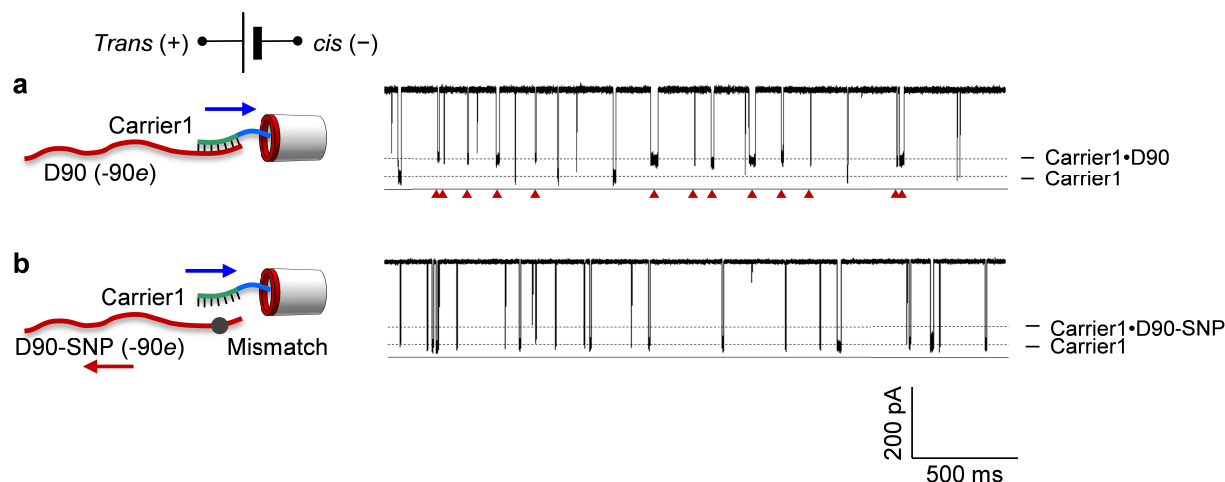
Figure S14. Detection of single nucleotide polymorphism using the carrier-assisted nanopore dielectrophoresis. **a-b,** Representative ionic current traces produced by the capture of Carrier1•DNA hybrids in the case of the DNA target D90 (a) and its variant D90-SNP (b). The current traces were recorded at +180 mV and equimolar (100 nM) mixtures of Carrier1 and either fully matched D90 target or D90-SNP variant that contained one mismatched basepair (Table S1). In panel a, the blockades produced by the carrier•DNA complex are marked by solid triangles. In panel b, the frequency of such high-conductance blockades, which would indicate the capture of Carrier1•D90-SNP complexes, is greatly reduced. The pronounced reduction of the high-conductance blockades in the case of the D90-SNP target demonstrated single-nucleotide sensitivity of the carrier-assisted nanopore dielectrophoresis. The block current amplitude (I) - duration (τ_{off}) scatter plots for D90 and D90-SNP are shown in Fig. 4 in the main text.

←— DNA template (sense strand, 65-nt)

←— APOC1_41 (RNA product, 41-nt)
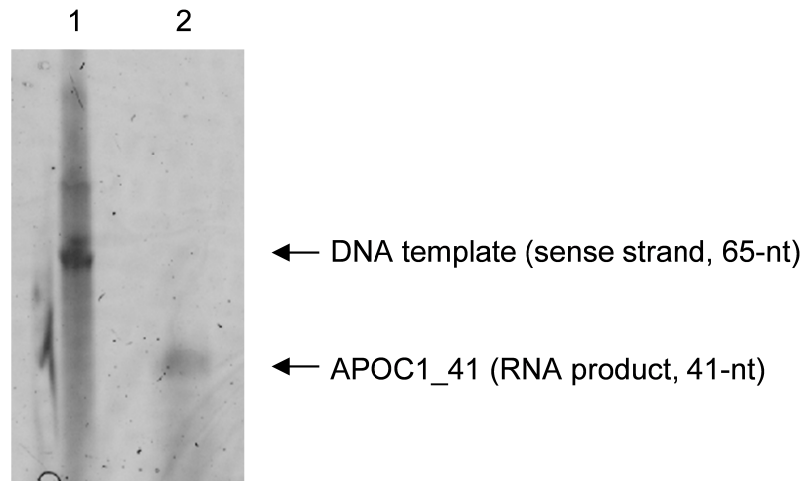
Figure S15. Gel electrophoresis images showing the *in vitro* transcription of RNA product. The bands in the two lanes and the corresponding samples are: Lane 1, 65-nt sense strand of the DNA template for the RNA synthesis; Lane 2, 41-nt RNA APOC1_41 synthesized by *in vitro* transcription. Electrophoresis condition: 12% polyacrylamide gel (19:1) in 8 M urea, 300 V, 4 °C, 2 hrs.

Supplementary Methods 1: Materials, RNA synthesis and processing, and single channel recording

Chemicals and materials. All DNA constructs, including target DNA (Table S1) and primer DNA for mutant αHL construction were synthesized and electrophoresis-purified by Integrated DNA Technologies (Coralville, IA). The peptide-PNA carriers (Table S1) were synthesized and HPLC-purified by Bio-Synthesis Inc (Lewisville, TX) with a purity of 95%. All polymers were dissolved in RNAase-free water to 100 µM as stocks. Prior to the nanopore measurement, the target nucleic acids, carrier and their mixtures at desired concentrations were heated to 90 °C for 5 minutes, then gradually cooled down to room temperature. Lipid 1, 2-diphytanoyl-sn-glycerophosphatidylcholine (DPhPC) was purchased from Avanti Polar Lipids (Alabaster, AL). The 25-µm-thick Teflon film was obtained from Goodfellow Inc (Oakdale, PA). The mutant α-hemolysin proteins $K131D_7$ and $K131N_7$ were constructed according to a method as described elsewhere.[1] The wild-type and mutant proteins were synthesized using the *in vitro* Transcription and Translation kit from Promega Corporation (Madison, WI), and collected from the electrophoresis gel.[2]

RNA *in vitro* transcription, purification and hybridization with carrier. RNA target APOC1-41 (Table S1) was synthesized by *in vitro* transcription.[3] The transcription template dsDNA was, sense strand: 5'-GAA ATT AAT ACG ACT CAC TAT AGG GCA GCC TAG CAA TGT CAC TAT GCT ACA CTT TTC CTA GTG TG-3'; and antisense strand: 5'-CAC ACT AGG AAA AGT GTA GCA TAG TGA CAT TGC TAG GCT GCC CTA TAG TGA GTC GTA TTA ATT TC-3'. The fragment from position 1 (G) to 24 (G) in the sense strand is the promotor. The RNA synthesis started from position 25 (G). The 100 µL *in vitro* transcription reaction system was a mixture of 6 µL of template DNA (total 20 pmol), 2 µL of 50,000

units/mL T7 RNA polymerase (New England Biolabs, M0251S), 2.5 μL of 2,000 units/mL inorganic pyrophosphatase (IPP, New England Biolabs, M0296S), 5 μL of 40 mM NTPs (Thermo Fisher Scientific, 18109-017), 10 μL of 10× reaction buffer, and 74.5 μL RNase-free water. The system was incubated at 37 °C for 2 h to synthesize RNA, then mixed with 20 μL of DNase I at 37 °C for 30 min to digest template DNA, and finally mixed with 50 μL of 0.5 mM EDTA to terminate the digestion. The RNA product was resolved in 12% urea (8 M)-denaturing polyacrylamide gel at 300 V and 4 °C for 2 h (Fig. S15). The RNA band was cut under the short wavelength UV light, then crushed and incubated in 2 volume (v/v) crush and soak buffer overnight. RNA was precipitated by ethanol, re-dissolved in RNase-free water, and finally quantified in NanoDrop 2000 (Thermo Scientific). Long RNAs may fold into tertiary structures. Folded RNA may change the carrier•RNA dipole structure and affect the capture efficiency. In our pre-treatment, instead of the slow continuous cooling process, the carrier/APOC1-41 mixture was first heated at 94℃ for 10 min, and then it was held at 50℃ for 10 min, 37℃ for 10 min, and 22℃ for 30 min. This RNA treatment can greatly enhance the capture efficiency. The stepwise cooling process likely reduces RNA folding prior to hybridization with the nanocarrier.

Electrophysiology recordings from single protein pores. Nanopore electrical recording was conducted according to previously reported protocols.[4] Briefly, the lipid bilayer membrane was formed over a 100-150 µm orifice in the center of the Teflon film that partitioned between *cis* and *trans* recording solutions. Both solutions contained KCl at a desired concentration (1 M) and were buffered with 10 mM Tris (pH 7.2). The alpha-hemolysin proteins were added to the *cis* solution, from which they inserted into the bilayer to form a nanopore. Nucleic acids, carriers, and their mixtures were added to the *trans* solution. The voltage was applied to the *trans* solution while the *cis* solution was grounded. In this setup, a positive voltage pulls a positively charged

carrier and the carrier•nucleic acids complex into the pore from the *trans* entrance. The ionic current through the pore was recorded using an Axopatch 200B amplifier (Molecular Device Inc., Sunnyvale, CA), filtered with a built-in 4-pole low-pass Bessel Filter at 5 kHz, and acquired with Clampex 9.0 software (Molecular Device Inc.) through a Digidata 1440 A/D converter (Molecular Device Inc.) at a sampling rate of 20 kHz. All current traces shown in figures were truncated from long recordings from 30 minutes to 1 hour. Data of single-channel event amplitudes and durations was collected using Clampfit 9.0 (Molecular Device Inc.) and analyzed using Clampfit, Excel (Microsoft) and SigmaPlot (SPSS) software. The nanopore measurements were conducted at 22 ± 2 °C. Data were presented as mean $\pm$ SD of at least three independent experiments.

Supplementary Methods 2: MD protocols

All MD simulations were performed using the NAMD2 program,[5] a 2 fs integration timestep, 2-2-6 multiple time stepping, CHARMM27 force field,[6] custom NBFIX corrections to describe ion-DNA interactions,[7] and periodic boundary conditions. A van der Waals cutoff of 7-8 Å was used for short-range forces, and the Particle Mesh Ewald[8] method over a 1.2 Å grid was employed for long-range electrostatic forces. Atoms within 3 bonds of one another were excluded from non-bonded interactions. Water molecules were held rigid using the SETTLE algorithm;[9] all other covalent bonds involving a hydrogen atom were held rigid using the RATTLE algorithm.[10] All equilibration simulations were performed in the constant area, number of particles, pressure and temperature ensemble. The area of the simulation system parallel to the plane of the lipid bilayer was kept fixed, the system's individual dimensions were subject to a langevin piston set to 1 atm target pressure with a decay and period of 800 fs each. Temperature was set to 295 K *via* the Lowe-Anderson thermostat[11] with a rate of 40 ps^{-1} and cutoff of 2.7 Å. The Visual Molecular Dynamics (VMD) program[12] was used for visualization and data analysis purposes.

All-atom models of the experimental system were built starting from a previously described model[13] of αHL embedded in a POPC bilayer and surrounded by 1 M KCl solvent. The WT[13] and the mutant $K131D_7$ open-pore systems contained approximately 288,700 atoms. The mutant system was minimized for 2400 steps using a conjugate gradient method to eliminate steric conflicts.

More systems were created by adding three varieties of probes to the existing open pore systems. The first, a polypeptide probe, was taken from an existing model (PDB ID 1JFW) and truncated to sequence N-YGRKKRRQRRR-C. The second, an ssDNA probe, was based on an

equilibrated conformation of ssDNA obtained previously,[14] modified to have the 5′-CCCGACATAGC-3′ nucleotide sequence. The probes were placed near the *trans* entrance of the αHL pore in several orientations (Fig. 2e and Fig. S10). Water and ions were added to increase the size of the simulation system along the pore's axis. The resulting systems contained approximately 315,500 atoms.

To build the third probe, the carrier•DNA complex, the peptide tag (described above) was appended to the C-terminal of the peptide nucleic acid (PNA) fragment of the 8-basepair PNA-DNA duplex.[15] The DNA strand of the PNA-DNA duplex was extended to 28 nucleotides by attaching a poly(dC)$_{20}$ fragment to the 5′ end of the duplex. The total charge of the resulting peptide-PNA-ssDNA probe was -19e,; the nucleotide sequence of the DNA part of the probe was 5'-CCCCCCCCCCCCCCCCCCCGACATAGC-3'. Parameters for simulating PNA, a molecule formed of DNA bases linked by amide bonds, were identical to those used in a previous work[16] except at the interface between PNA and the peptide: the bond between PNA and peptide was described as the standard inter-peptide bond of CHARMM27. Imprecisions in the initial bond lengths and positions of the molecular fragments were eliminated through 1200 steps of minimization of the hybrid probe in solvent. The carrier•DNA probe was added to the open pore systems in the conformation shown in Fig. 2a. Including added solvent, the ssDNA-PNA-peptide tag systems contained approximately 370,000 atoms.

Each probe-hemolysin system was minimized for 2400 steps after the probe insertion to eliminate steric conflicts, with heavy atoms under harmonic restraints of 0.5 kcal mol^{-1} Å^{-2}. Following minimization, each system was equilibrated for 1 ns. The average size of the system obtained within the last 0.6 ns of equilibration was used in the subsequent simulations under

applied electric field, which were performed in the constant number of particles, volume and temperature ensemble. In each simulation, harmonic restraints were applied to all alpha-carbon atoms of alpha-hemolysin with restraint coordinates matching the initial structure.[13] Harmonic constraints used spring constants of 0.5 kcal mol^{-1} Å^{-2}. Electric field simulations were performed with electric field strength given by $E = -V/Lz$, where V is the desired transmembrane bias and Lz is the length of the system in the direction of the field[17]

Supplementary Methods 3: Theoretical model of nanopore dielectrophoresis

Q Amount of negative charge at the entrance of nanopore

z z-coordinate of a testing point

d Pore diameter

L Pore length

r Distance from a testing point to pore charge Q ($r = \sqrt{z^2 + (d/2)^2}$),

κ^{-1} Debye length ($\kappa^{-1} = \sqrt{\frac{\varepsilon_0 \varepsilon k_B T}{2e^2 C N_A}}$ for monovalent electrolyte such as KCl)

k_B Boltzmann constant (1.38×10^{-23} J·K^{-1})

C Electrolyte (KCl) concentration (in mole per m^3)

T Temperature (K)

N_A Avogadro constant (6.02×10^{-23} mole^{-1})

e Elementary charge (1.6×10^{-19} C)

ε_0 Vacuum permittivity (8.85×10^{-12} C·V^{-1}·m^{-1})

ε Relative permittivity (80 in water)

k Coulomb's constant, $k = 1/4\pi\varepsilon_0 = 9 \times 10^9$ N·m^2·C^{-2}

        Non-uniform electric field contributed by the nanopore charge and voltage bias. The electric field around the nanopore entrance is mainly contributed by the local charged residues. The principle is demonstrated in Box. 1. We assume that the nanopore has been engineered to have negatively charged amino acids such as aspartic acids placed at its entrance. The total

charge of these residues is Q and the residues are assembled a uniformly distributed "Q-ring" along the edge of the pore entrance. The electrostatic potential distribution produced by the charge Q can be expressed as

$$U_Q(r) = \frac{kQ}{\varepsilon r} e^{-r/\kappa^{-1}} \qquad (S1)$$

where k is the Coulomb's constant, ε is the relative permittivity (ε=80 in water), r is the distance from the test point to the pore charge Q. The exponential factor in Eq. S1 describes the charge screening effect in high salt concentration, where κ^{-1} is the Debye length and κ^{-1}=0.3 nm in 1 M KCl. The electric field intensity distribution $E_Q(r)$ generated by Q can be obtained as a derivative of the potential $U_Q(r)$,

Box. 1

a, Evaluation of the electric field strength distribution outside the pore entrance produced by the negatively charged residues engineered at the pore entrance and voltage bias; **b.** Evaluation of the effective force $F(z)$ on a carrier•DNA complex placed in the field.

$$E_Q(r) = \frac{dU_Q(r)}{dr} = \frac{-kQ}{\varepsilon}\left(\frac{1}{r^2} + \frac{1}{r\kappa^{-1}}\right)e^{-\frac{r}{\kappa^{-1}}} \qquad (S2)$$

$E_Q(r)$ is a vector. Because of the cylindrical symmetry of the system, $E_Q(r)$ can be represented as a sum of a component $E_Q(z)$ that is parallel to the z-axis and a component that is normal to the z-axis. Because Q is uniformly distributed on the "charge ring" at the pore entrance, the normal-to-z component of $E_Q(r)$ along the pore axis is zero, and only the $E_Q(z)$ component provides the driving force along the z axis. If z is the z-axis coordinate of the test point and d is the pore
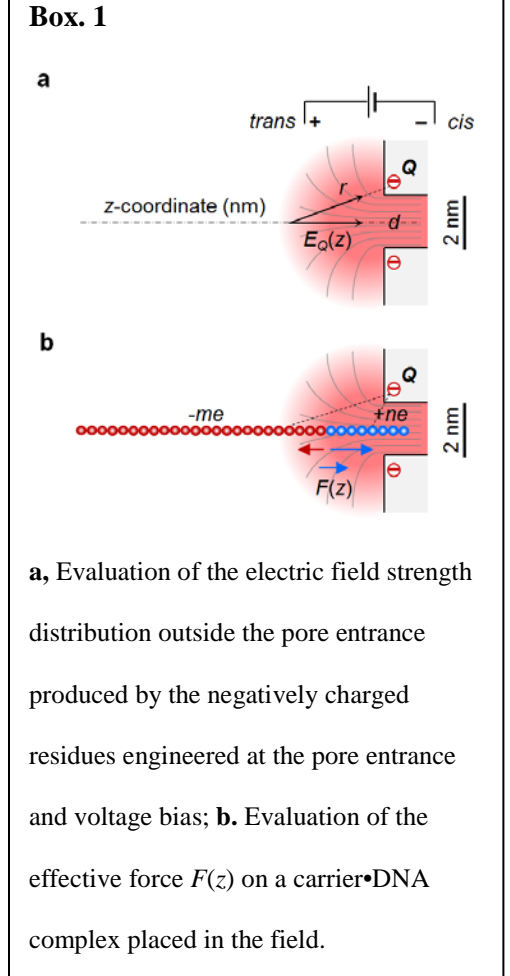
diameter (d=2 nm for the α-hemolysin pore), the r-z relation is $r = \sqrt{z^2 + (d/2)^2}$. Therefore the $E_Q(r)$ component along the z-axis can be expressed as

$$E_Q(z) = E_Q(r)\frac{z}{r} \qquad (r = \sqrt{z^2 + (d/2)^2}) \qquad \text{(S3)}$$

By combining Eq. S2 and Eq. S3, we obtained the final expression of $E_Q(z)$

$$E_Q(z) = \left[\frac{-kQ}{\varepsilon}\left(\frac{1}{r^2} + \frac{1}{r\kappa^{-1}}\right)e^{-\frac{r}{\kappa^{-1}}}\right]\frac{z}{r} \qquad \left(r = \sqrt{z^2 + (d/2)^2}\right) \qquad \text{(S4)}$$

In addition to the charges at the pore entrance, the voltage V across the pore can contribute to the electric field outside the pore entrance E_V. If the pore length is l, E_V inside the pore would be V/l. This field sharply decays as being away from the pore, with a distribution $E_V(z)=\nabla V(z)$, where $V(z)$ is the potential profile outside the pore. In a previous study,[18] $V(z)$ was found to be inversely proportional to z, i.e. $V(z) \sim 1/z$, with a constant factor $Vd^2/8L$. Thus $E_V(z)$ decays in inverse proportion to z^2, i.e. $E_V(z) \sim 1/z^2$. Taking the boundary condition into consideration, i.e. $E_V(0)=V/l$ at the pore entrance (z=0), we obtain the expression for $E_V(z)$ as

$$E_V(z) = \frac{Vd^2}{8l\left(z - \frac{d}{2\sqrt{2}}\right)^2} = E_V(0)\frac{1}{\left(2\sqrt{2}z/d - 1\right)^2} \quad (z \le 0) \qquad \text{(S5)}$$

The sum of $E_Q(z)$ and $E_V(z)$ gives the total field intensity distribution,

$$E(z) = E_V(z) + E_V(z) \qquad \text{(S6)}$$

In Fig. S12b, we used Eqs. S4-S6 to compare $E(z)$ for various Q. Specifically, Q=−21e represented the K131D$_7$ pore, which contains 7 copies of D127(−), D128(−), and D131(−); Q=−14e corresponded to the K131N pore carrying 7 copies of D127(−) and D128(−); Q=−7e was for the wild-type (WT) pore with 7 copies of D127(−), D128(−) and K131(+); and Q=0 was

for the pore whose field was only generated by the voltage. The $E(z)$ curves in Fig. S12b indicate that $E(z)$ at $z<0$ significantly changes with Q, suggesting that the charge at the pore entrance is a critical contributor to the field outside the pore. In Fig. S13a, we used Eqs. S4-S6 to compare $E(z)$ at 100 and 200 mV. In contrast to the E-Q relationship, $E(z)$ at $z<0$ modestly changes with the voltage, but $E(z)$ at $z>0$ significantly varied with the voltage, suggesting that the voltage moderately contributes to the field outside the pore, but is a dominant source of the field inside the pore.

Effective force on the carrier•DNA complex placed in the field. As shown in Box. 1, the carrier contains n cationic amino acids appended to a neutral PNA tail that binds to m nucleotides of the target nucleic acid. To evaluate the effective force $F(z)$ on the carrier•DNA complex in the non-uniform field $E_Q(z)$ (described above), we treated the carrier•DNA complex as a string of n positive charges (for amino acids) linked with m negative charges (for nucleotides). We defined z_{+i} and z_{-j} as the z-coordinates of the ith amino acid and the jth nucleotide. When placed in the field $E_Q(z)$, each positive charge is attracted toward the pore by a force $eE_Q(z_{+i})$, and each negative charge is repelled from the pore by a force $-eE_Q(z_{-j})$. The sum of these forces is the effective electrostatic force $F(z)$ experienced by the entire carrier•DNA complex,

$$F(z) = \sum_{i=1}^{n} eE_Q(z_{+i}) - \sum_{j=1}^{m} eE_Q(z_{-j}) \qquad (S7)$$

If z_{+1} is the z-coordinate of the 1st positively charged amino acid, and d_+ is the distance between adjacent amino acids in a polypeptide (d_+=0.3 nm), the z-coordinate of each amino acid z_{+i} is

$$z_{+i} = z_{+1} - (i-1)d_+ \qquad (S8)$$

If z_{-1} is the coordinate of the 1st nucleotide immediately following the last (n^{th}) amino acid of the polypeptide, $z_{-1} = z_{+1} - (n-1)d_+$. If d_- is the distance between adjacent nucleotides in ssDNA ($d_-=0.6$ nm), the coordinate of each nucleotide $z_{-j} = z_{-1} - (j-1)d_-$. Overall, the coordinate of the jth nucleotide as a function of that of the 1st amino acid (z_{+1}) is

$$z_{-j} = z_{+1} - (n-1)d_+ - (j-1)d_- \qquad \text{(S9)}$$

As the polymer moves in the field toward the pore, we can calculate the field-generated force acting on each charged unit (amino acid or nucleotide) according to its z-coordinate, and obtain the effective force $F(z)$ acting on the entire carrier•DNA complex.

In Fig. S12d, we used Eqs. S7-S9 to calculate the effective force $F(z)$ acting on various carrier•DNA complexes. $F(z)$ is plotted as a function of the z-coordinate of the 1st amino acid (z_{+1}). First, we consider the case of eight cationic amino acids ($n=8$, $+8e$) bound to a 50 nucleotide ssDNA ($m=50$, $-50e$). Although the net charge of the complex is highly negative, the calculations suggest an attractive force ($F(z)>0$) on the carrier•DNA complex as it moves in the field $E_Q(z)$ (Fig. 2c). The attractive force emerged when the 1st cationic amino acid of the carrier was a couple of nanometer away from the pore. The attractive force increased as the carrier•DNA complex moves toward the pore, and reaches a maximum when the 1st cationic residue is placed at the pore entrance. Such behavior of $F(z)$ is consistent with the results of MD simulations in Fig. 2c. Note that the definition of the z-coordinate for the force profiles shown in Fig. S12c and Fig. 2c are different. In Fig. S12c, $F(z)$ is presented versus the z-coordinate of the 1st cationic amino acids of the complex, whereas in Fig. 2c, $F(z)$ is presented as the function of Center of Mass (CoM) of the carrier•DNA complex, which is located about 2-3 nm away from the 1st cationic amino acid of the carrier. Therefore the results of the MD simulation and electrostatic analysis are in agreement with each other.

We have also used Eqs. S7-S9 to analyze $F(z)$ acting on the carrier•DNA complexes for DNA targets of different length. In this analysis, the carrier contained eight positive residues ($+8e$), whereas ssDNA targets contained 10, 50 and 90 nucleotides ($-10e$, $-50e$, and $-90e$). As shown in Fig. S12d, $F(z)$ for all carrier•DNA complexes were almost identical and overlapped with each other. This result is consistent with the experimentally observed independence of the carrier•DNA capture rate on the DNA length. Indeed, for a long DNA, only a few nucleotides most proximal to the cationic peptide would experience the field, as the rest of the nucleic acid strand, no matter how long, would extend into the bulk solution where the field decays to zero and therefore would not contribute to the effective force $F(z)$.

References

1. Howorka, S.; Bayley, H. Improved Protocol for High-Throughput Cysteine Scanning Mutagenesis. *Biotechniques* **1998**, *25*, 764-766.

2. Cheley, S.; Braha, O.; Lu, X.; Conlan, S.; Bayley, H. A Functional Protein Pore with a "Retro" Transmembrane Domain. *Protein Sci.* **1999**, *8*, 1257-1267.

3. Cazenave, C.; Uhlenbeck, O. C. RNA Template-Directed RNA Synthesis by T7 RNA Polymerase. *Proc. Natl. Acad. Sci. U. S. A.* **1994**, *91*, 6972-6976.

4. Braha, O.; Walker, B.; Cheley, S.; Kasianowicz, J. J.; Song, L.; Gouaux, J. E.; Bayley, H. Designed Protein Pores as Components for Biosensors. *Chem. Biol.* **1997**, *4*, 497-505.

5. Phillips, J. C.; Braun, R.; Wang, W.; Gumbart, J.; Tajkhorshid, E.; Villa, E.; Chipot, C.; Skeel, R. D.; Kale, L.; Schulten, K. Scalable Molecular Dynamics with Namd. *J. Comput. Chem.* **2005**, *26*, 1781-1802.

6. MacKerell, A. D.; Bashford, D.; Bellott, M.; Dunbrack, R. L.; Evanseck, J. D.; Field, M. J.; Fischer, S.; Gao, J.; Guo, H.; Ha, S.; Joseph-McCarthy, D.; Kuchnir, L.; Kuczera, K.; Lau, F. T.; Mattos, C.; Michnick, S.; Ngo, T.; Nguyen, D. T.; Prodhom, B.; Reiher, W. E.*, et al.* All-Atom Empirical Potential for Molecular Modeling and Dynamics Studies of Proteins. *J. Phys. Chem. B* **1998**, *102*, 3586-3616.

7. Yoo, J.; Aksimentiev, A. Improved Parametrization of Li^+, Na^+, K^+, and Mg^{2+} Ions for All-Atom Molecular Dynamics Simulations of Nucleic Acid Systems. *J. Phys. Chem. Lett.* **2012**, *3*, 45-50.

8. Darden, T.; York, D.; Pedersen, L. Particle Mesh Ewald: An N·Log(N) Method for Ewald Sums in Large Systems. *J. Chem. Phys.* **1993**, *98*, 10089-10092.

9. Miyamoto, S.; Kollman, P. A. Settle: An Analytical Version of the Shake and Rattle Algorithm for Rigid Water Models. *J. Comput. Chem.* **1992**, *13*, 952-962.

10. Andersen, H. C. Rattle: A "Velocity" Version of the Shake Algorithm for Molecular Dynamics Calculations. *J. Comput. Phys.* **1983**, *52*, 24-34.

11. Koopman, E. A.; Lowe, C. P. Advantages of a Lowe-Andersen Thermostat in Molecular Dynamics Simulations. *J. Chem Phys.* **2006**, *124*, 204103.

12.   Humphrey, W.; Dalke, A.; Schulten, K. Vmd: Visual Molecular Dynamics. *J. Mol. Graph.* **1996**, *14*, 33-38, 27-38.

13.   Bhattacharya, S.; Muzard, J.; Payet, L.; Mathé, J.; Bockelmann, U.; Aksimentiev, A.; Viasnoff, V. Rectification of the Current in Alpha-Hemolysin Pore Depends on the Cation Type: The Alkali Series Probed by Molecular Dynamics Simulations and Experiments. *J. Phys. Chem. C* **2011**, *115*, 4255-4264.

14.   Bhattacharya, S.; Derrington, I. M.; Pavlenok, M.; Niederweis, M.; Gundlach, J. H.; Aksimentiev, A. Molecular Dynamics Study of MspA Arginine Mutants Predicts Slow DNA Translocations and Ion Current Blockades Indicative of DNA Sequence. *ACS Nano* **2012**, *6*, 6960-6968.

15.   Eriksson, M.; Nielsen, P. E. Solution Structure of a Peptide Nucleic Acid-DNA Duplex. *Nat. Struct. Biol.* **1996**, *3*, 410-413.

16.   Weroński, P.; Jiang, Y.; Rasmussen, S. Molecular Dynamics Study of Small PNA Molecules in Lipid-Water System. *Biophys. J.* **2007**, *92*, 3081-3091.

17.   Aksimentiev, A.; Schulten, K. Imaging Alpha-Hemolysin with Molecular Dynamics: Ionic Conductance, Osmotic Permeability, and the Electrostatic Potential Map. *Biophys. J.* **2005**, *88*, 3745-3761.

18.   Wanunu, M.; Morrison, W.; Rabin, Y.; Grosberg, A. Y.; Meller, A. Electrostatic Focusing of Unlabelled DNA into Nanoscale Pores Using a Salt Gradient. *Nat. Nanotechnol.* **2010**, *5*, 160-165.